

TIME-DEPENDENT TRANSONIC FLOW SOLUTIONS FOR AXIAL TURBOMACHINERY

By John Erdos, Edgar Alzner, Paul Kalben,
Advanced Technology Laboratories, Inc.

William McNally,
NASA Lewis Research Center
and Simon Slutsky
Polytechnic Institute of New York

SUMMARY

Three-dimensional unsteady transonic flow through an axial turbomachine stage is described in terms of a pair of two-dimensional formulations pertaining to orthogonal surfaces, namely, a blade-to-blade surface and a hub-to-casing surface. The resulting systems of nonlinear, inviscid, compressible equations of motion are solved by an explicit finite-difference technique. Separate computer programs have been constructed for each formulation. The blade-to-blade program includes the periodic interaction between rotor and stator blade rows. Treatment of the boundary conditions and of the blade slipstream motion by a characteristic type procedure is discussed in detail. Harmonic analysis of the acoustic far field produced by the blade row interaction, including an arbitrary initial transient, is outlined in an appendix. Results from the blade-to-blade program are compared with experimental measurements of the rotating pressure field at the tip of a high-speed fan. The hub-to-casing program determines circumferentially averaged flow properties on a meridional plane. Blade row interactions are neglected in this formulation, but the force distributions over the entire blade surface for both the rotor and stator are obtained. Results from the hub-to-casing program are compared with a relaxation method solution for a subsonic rotor. Results are also presented for a quiet fan stage designed by the National Aeronautics and Space Administration, which includes transonic flow in both the rotor and stator and a normal shock in the stator.

INTRODUCTION

Flow through a high-speed fan or compressor is highly three-dimensional and can include complex shock wave systems. In addition, flow through a complete stage consisting of a rotor and stator or a fan preceded by inlet guide vanes is unsteady even in the rotating frame of reference. Effects of viscosity and turbulence are known to be signifi-

cant; in fact, the turbulent wakes may be the predominant source of aerodynamic interaction between the rotating and stationary blade rows and responsible for the associated noise. Vortex filaments are known to stream from the rotor tips and undoubtedly interact with the wall boundary layer. Sufficiently far downstream, turbulence generated by the first blade row may encompass the entire flow. Calculation of transonic flow field solutions in high-speed turbomachinery stages is clearly one of the most formidable challenges to present-day capabilities in computational aerodynamics.

A traditional approach to solution of this complex problem has been taken. Description of the inviscid flow field is addressed first, boundary layer and turbulence effects being superimposed as small perturbations. The basic system of equations which is solved numerically consists of the complete nonlinear equations of motion for an inviscid compressible gas:

$$\frac{\partial \rho}{\partial t} + \nabla \cdot \rho \mathbf{V} = 0 \quad (1)$$

$$\frac{D\mathbf{V}}{Dt} = -\frac{1}{\rho} \nabla p \quad (2)$$

$$\frac{De}{Dt} + p \frac{D(\rho^{-1})}{Dt} = 0 \quad (3)$$

where

$$p = \rho RT \quad (4)$$

$$e = \frac{p}{(\gamma - 1)\rho} \quad (5)$$

$$\frac{D}{Dt} = \frac{\partial}{\partial t} + \mathbf{V} \cdot \nabla \quad (6)$$

and

e internal energy

p pressure

R gas constant

T temperature

t time

V velocity vector

ρ density

The only essential simplifications introduced pertain to reduction of the spatial dimensions of the problem from 3 to 2. Solution of the full three-dimensional problem is reduced to a pair of two-dimensional solutions on orthogonal surfaces. A separate program tailored to the particular aspects of each formulation has been developed. Both computer programs which will be discussed herein are intended for analysis of a complete stage, that is, rotor and stator, although an isolated blade row can also be treated.

A harmonic type analysis of the acoustic far field due to blade row interactions has also been developed. This analysis provides a direct coupling between the numerical near-field solution and the acoustic far field, with a particular view toward characterizing the acoustic far field. This aspect of the flow model will be only briefly outlined herein, but a complete description is given in reference 1. The boundary-layer and wake representations utilize standard integral methods and it is assumed that the boundary layer and wake are quasi-steady. The reader is again referred to reference 1 for a complete description.

SYMBOLS

A_n, B_n, C_n, \dots Fourier coefficients

a speed of sound

b stream sheet thickness or blade thickness

ϵ centerline

c chord

E total internal energy

e internal energy

H total enthalpy

h enthalpy

M Mach number

m	meridional distance along a blade-to-blade stream surface
N_i	number of blades in i th row
n	blade-to-blade distance
P, Q, R	boundary conditions at interface of numerical near-field and acoustic far-field solutions
p	pressure
R	gas constant
r	radial distance from axis of rotation
S	entropy
s	distance along the stream path
T	temperature
t	time
U	a reference velocity
u	meridional component of velocity
\bar{u}	velocity component parallel to slipstream or blade surface
V	velocity vector
v	circumferential component of velocity
\bar{v}	velocity component normal to slipstream or blade surface
v_r	radial component of velocity; also circumferential velocity component in rotating coordinate system
v_z	axial velocity component

v_θ	circumferential velocity component
x	meridional distance along a blade-to-blade stream surface
\bar{x}	distance along slipstream or blade surface
y	circumferential distance
\bar{y}	distance normal to slipstream or blade surface
z	axial coordinate
α_n, β_n	acoustic propagation coefficient
γ	ratio of specific heats
θ	circumferential angle
θ_1, θ_2	blade surface coordinates
ρ	density
ϕ	angle between slipstream or blade surface and meridional plane
ψ	ratio of mass flow to total mass flow
Ω	angular speed of rotor
ω	vorticity; also frequency

Subscripts:

o	initial or reference condition
$*$	reference condition
∞	free stream

A circumflex ($\hat{}$) over a symbol denotes an average value. A bar over a symbol denotes vector quantities except in appendix where it denotes time to frequency transform.

BLADE-TO-BLADE ANALYSIS

In the blade-to-blade formulation the previously stated equations of motion are expressed in a curvilinear coordinate system alined on an axisymmetric stream surface as shown in figure 1. This stream surface is considered to have small but finite thickness $b(z)$ and variable mean radius from the axis of rotation $r(z)$. The velocity component normal to the stream surface is neglected; as a result, a two-dimensional approximation to the flow field is produced. (See refs. 2 and 3.) When the m, θ coordinates are transformed to a rotating system by

$$x = m \quad (7)$$

$$y = r(\theta - \Omega t) \quad (x = \text{Constant}) \quad (8)$$

and the circumferential velocity component is transformed by

$$v_r = v - \Omega r \quad (9)$$

then the following system of governing equations result:

$$\frac{\partial \rho}{\partial t} + \frac{\partial}{\partial x}(\rho u) + \frac{\partial}{\partial y}(\rho v_r) = -\frac{\rho u}{rb} \frac{drb}{dx} \quad (10)$$

$$\frac{\partial \rho u}{\partial t} + \frac{\partial}{\partial x}(\rho u^2 + p) + \frac{\partial}{\partial y}(\rho u v_r) = -\frac{\rho u^2}{rb} \frac{drb}{dx} \quad (11)$$

$$\frac{\partial \rho v_r}{\partial t} + \frac{\partial}{\partial x}(\rho u v_r) + \frac{\partial}{\partial y}(\rho v_r^2 + p) = -\frac{\rho u v_r}{rb} \frac{drb}{dx} - \rho u \Omega \frac{dr}{dx} \quad (12)$$

$$\frac{\partial \rho E_r}{\partial t} + \frac{\partial}{\partial x}(\rho u H_r) + \frac{\partial}{\partial y}(\rho v_r H_r) = -\frac{\rho u H_r}{rb} \frac{drb}{dx} - \rho u \Omega \frac{dr}{dx} (\Omega r + v_r) \quad (13)$$

where the relative total energy and total enthalpy are defined by

$$H_r = H - \Omega r v \quad (14)$$

$$E_r = H_r - \frac{p}{\rho} \quad (15)$$

The terms on the right-hand side of the equations result from the variations in cross-sectional area and radius of the stream surface, which are intended to account for the effects of variations in hub and casing radii. The terms on the left-hand side of the equations correspond to the familiar set of two-dimensional unsteady equations of motion

of an inviscid compressible gas. Note that the relative total enthalpy is not the same as the total enthalpy defined on the basis of velocity components in the rotating frame. Numerical solution of this system of equations at interior grid points is accomplished by the MacCormack algorithm (ref. 4). Systematic rotation of the order in which the non-centered differences are evaluated is employed to minimize any bias in the solution due to the alternating directions of the noncentered differences. No artificial damping or stabilization is used.

As shown in figure 1, the computational domain is divided into a maximum of seven segments, not all of which need be included in every case. The grid network extends axially from an inlet station to a discharge station and circumferentially across one blade-to-blade passage. The inlet station is located either 1 axial chord length upstream of the first blade row, in which case domain 1 is deleted, or an arbitrary distance upstream exceeding 1 chord length. Placement of the discharge station can be selected in the same manner as that employed for the inlet station. Domains 2 to 6 are each linearly mapped into a unit square which is spanned by a rectangular grid network. In domains 1 and 7 a linear stretching of the axial coordinate is used to map these domains into unit squares. The axial grid spacing in domains 1, 4, and 7 is determined by the locations of the axial boundaries of these domains. The lateral boundaries of domains 1 and 2 lie on extensions of the mean camber line. The lateral boundaries of domains 3 and 5 lie on the blade surfaces. The instantaneous locations of the blade slipstreams form the boundaries of domains 4, 6, and 7. Domains 1 to 4 are attached to the first blade row and domains 5 to 7 are attached to the second blade row either of which may be selected as the rotating row. It is assumed that the number of blades in the second row equals or exceeds the number in the first row.

It is emphasized that a periodic solution due to the aerodynamic interaction of the rotating and stationary blades is anticipated. The formulation is thus a numerical counterpart of the problem for which Kemp and Sears (ref. 5) obtained an analytic solution pertaining to thin, slightly cambered blades of low solidity in an incompressible flow. Linearized solutions have more recently been obtained for compressible flows, but the authors are not aware of any other attempt to develop nonlinear solutions for the periodic blade-row interaction problem at transonic or supersonic conditions.

In connection with the periodicity of the subject problem, two main points of departure from other numerical solutions for transonic airfoils or cascades should be recognized. First, the slipstreams are moving surfaces of discontinuity across which jumps in tangential component velocity and in total pressure can occur. Only static pressure and the component of velocity normal to the surface must be continuous. It should be noted that the jumps in tangential velocity across the slipstreams are related to the unsteady variations in lift of the blades and therefore cannot be obtained from the conservation form of the equations of motion through a limiting process as in the case of

shock waves. Treatment of the slipstreams as surfaces of discontinuity in the present model is therefore warranted for two reasons: It allows attainment of an accurate periodic solution without requiring a very large grid point density to approximate the slipstream discontinuities, and tracking of the slipstreams is necessary to determine the trajectories of the viscous wakes which diffuse outward from the inviscid slipstreams. The second point is that in the case of an unequal number of blades in the two rows, the angular period of the circumferential variations in the flow field is not the width of a blade-to-blade passage but it is the circumference divided by the difference between the number of blades in the rotor and stator. Furthermore, the flow pattern rotates with an angular velocity which, in general, is a multiple of the wheel speed. Numerical representation of this periodicity condition pertaining to the lateral boundary points of the grid network, as well as to those points along the interface between domains 4 and 5, is accomplished by a cyclic procedure which is discussed later.

BOUNDARY CONDITIONS

The calculation of boundary points and indeed the exposition of proper boundary conditions is facilitated by recasting the equations in the form of characteristic compatibility relations pertaining to a quasi one-dimensional unsteady wave system (as suggested by Moretti and Abbett (ref. 6) and Serra (ref. 7)). Although actual numerical implementation of the characteristic formulation is far more complex than the finite-difference procedure used in the interior points and can possess certain drawbacks, such as inconsistency with the interior point solution, it is nevertheless adopted here for the particular advantages it offers with respect to the slipstream, inlet, and discharge point calculations.

Consider first the inlet station sketched in figure 2. As is well known, the momentum and energy equations can be rewritten in the form:

$$\frac{DS}{Dt} = 0 \quad \text{or} \quad S = \text{Constant} \quad \text{on} \quad \frac{\Delta x}{u} = \frac{\Delta y}{v_r} = \Delta t \quad (16)$$

$$\frac{D(\omega/\rho)}{Dt} = 0 \quad \text{or} \quad \frac{\omega}{\rho} = \text{Constant} \quad \text{on} \quad \frac{\Delta x}{u} = \frac{\Delta y}{v_r} = \Delta t \quad (17)$$

By assuming that no flow reversal occurs at the inlet station, the values of the entropy and ratio of vorticity to density at the inlet station are, therefore, solely properties of the incoming flow and may be specified a priori; both the entropy and vorticity of the incoming flow are assumed to be zero. Three options have been considered with regard to physical interpretation of the inlet boundary conditions. First, if the inlet station represents an open end of a finite length duct, the static pressure can be specified as

$$p = p_{-\infty} \quad (18a)$$

Second, if it is an arbitrary station in a duct of infinite length, the Riemann invariant on the downstream traveling wave can be specified as

$$\frac{2a}{\gamma - 1} + u = \frac{2a_{\infty}}{\gamma - 1} + u_{\infty} \quad (18b)$$

Use of this relationship implies that the outward traveling waves are one-dimensional (i.e., either planes or helices). As a third option the numerical solution can be matched to the acoustic far-field analysis at the inlet station, in which case all acoustic modes are properly accounted for. This procedure is outlined in an appendix. In any of these cases the solution of the inlet boundary points is completed by first using a compatibility relation on the upstream running wave which originates within the computational domain at point C in figure 2; that is,

$$\frac{a}{\gamma} \Delta \log p - \Delta u = \left[(v_r - v_0) \left(\frac{\partial u}{\partial y} - \frac{a}{\gamma} \frac{\partial \log p}{\partial y} \right) - a \frac{\partial v_r}{\partial y} - ua \frac{d \log rb}{dx} \right] \Delta t$$

(on $\frac{\Delta x}{\Delta t} = u - a$ and $\frac{\Delta y}{\Delta t} = v_0$) (19)

and second by solving the following angular momentum equation, which only involves spatial derivatives of the dependent variables in the circumferential direction, by the MacCormack finite-difference algorithm:

$$\frac{\partial v_r}{\partial t} = - \left(u \frac{\partial u}{\partial y} + v_r \frac{\partial v_r}{\partial y} + \frac{1}{\rho} \frac{\partial p}{\partial y} + u \Omega \frac{dr}{dx} \right) \quad (20)$$

This characteristic compatibility relation may be interpreted as pertaining to the projection of the true characteristic conoid on a reference plane which is aligned normal to the inlet station and translates in the circumferential direction with an arbitrary velocity v_0 , for example, v_r from the previous time step. The acoustic far-field analysis can be used to replace equation (18a) or (18b).

A similar procedure is employed at the discharge boundary points but here the entropy and vorticity are determined by tracing a particle path from within the computational domain (point B in fig. 2) to the boundary point. The system of equations pertaining to a discharge boundary point are stated below for the case of either a finite length duct or an infinite duct

$$p = p_{\infty} \quad (21a)$$

$$\frac{2a}{\gamma - 1} - u = \frac{2a_{\infty}}{\gamma - 1} - u_{\infty} \quad (21b)$$

Use of the acoustic model would replace equation (21a) or (21b)

$$\left. \begin{aligned} S &= S_* \\ \frac{\omega}{\rho} &= \frac{\omega_*}{\rho_*} \end{aligned} \right\} \quad \left(\text{on } \frac{\Delta x}{u} = \frac{\Delta y}{v} = \Delta t \right) \quad (22)$$

$$\frac{a}{\gamma} \Delta \log p + \Delta u = \left[-(\mathbf{v}_r - \mathbf{v}_o) \left(\frac{\partial u}{\partial y} + \frac{a}{\gamma} \frac{\partial \log p}{\partial y} \right) - a \frac{\partial \mathbf{v}_r}{\partial y} - u a \frac{d \log r b}{dx} \right] \Delta t$$

$$\left(\text{on } \frac{\Delta x}{\Delta t} = u + a \quad \text{and} \quad \frac{\Delta y}{\Delta t} = v_o \right) \quad (23)$$

$$\frac{\partial v}{\partial t} = - \left(u \frac{\partial u}{\partial y} + v_r \frac{\partial \mathbf{v}_r}{\partial y} + \frac{1}{\rho} \frac{\partial p}{\partial y} + 2\rho u \frac{\omega_*}{\rho_*} + u\Omega \frac{dr}{dx} \right) \quad (24)$$

The boundary condition at the blade surface points is simply vanishing of the component of velocity normal to the surface. At the trailing edge the Kutta condition is satisfied by requiring the pressure to be continuous and the velocity component normal to the mean of the camber line and slipstream to be zero. On the slipstream the pressure and normal component of the velocity must be continuous. Implementation of these conditions is facilitated by recasting the equations into a characteristic form similar to that described; however, in this case the reference planes are normal to the surface and translate in the streamwise direction, as shown in figure 3. Combination of the continuity equation and normal momentum equation results in the following pair of compatibility relations:

$$a \Delta \log p \pm \gamma \Delta \bar{v}_r = (aQ_1 \pm \gamma Q_2) \Delta t \quad \left(\text{on } \frac{\Delta \bar{y}}{\Delta t} = \bar{v}_r \pm a \quad \text{and} \quad \frac{\Delta \bar{x}}{\Delta t} = \bar{u}_o \right) \quad (25)$$

where

$$Q_1 = - \left[(\bar{u} - \bar{u}_o) \frac{\partial \log p}{\partial \bar{x}} + \frac{\partial \bar{u}}{\partial \bar{x}} + \gamma u \frac{d \log r b}{dx} \right] \quad (26)$$

$$Q_2 = - \left[(\bar{u} - \bar{u}_o) \frac{\partial \bar{v}_r}{\partial \bar{x}} - u\Omega \cos \phi \frac{dr}{dx} \right] \quad (27)$$

The energy equation is stated as

$$\left. \begin{aligned} \frac{DS}{Dt} &= 0 \\ S &= \text{Constant} \end{aligned} \right\} \quad \left(\text{on } \Delta \bar{x} = \bar{u} \Delta t \quad \text{and} \quad \Delta \bar{y} = \bar{v} \Delta t \right) \quad (28)$$

and the streamwise momentum equation is solved in the LaGrangian form

$$\frac{D\bar{q}}{Dt} = -\frac{a^2}{\gamma} \frac{\partial \log p}{\partial s} - \frac{uv_r}{q} \Omega \frac{dr}{dx} \quad (29)$$

where $\bar{q}^2 = \bar{u}^2 + \bar{v}^2$ and $ds/\bar{q} = d\bar{x}/\bar{u} = d\bar{y}/\bar{v} = dt$.

It is pointed out that the form of the compatibility relations given by equation (25) provides an algebraic solution for the quantities which are continuous across the blade slipstream, namely, the pressure and normal velocity. Thus, the boundary conditions on the blade slipstream can be satisfied without iteration, other than that necessary to locate the characteristic geometrically (points A and D in fig. 3) by successive approximations, of which two are usually sufficient. However, at the trailing edge an iteration is required to determine the slipstream angle which satisfies the Kutta condition.

The overall scheme for imposing the boundary conditions along the blade surface and slipstream points is shown schematically in figure 4. The time axis projects vertically out of the page in this figure. The dashed lines represent the intersections of the translating reference planes with the axisymmetric stream surface and the intersections of the particle paths with the stream surface during a time step Δt .

PERIODICITY CONDITION

Illustration of the nature of the cyclic procedure devised to enforce the periodicity of the solution can best be accomplished with respect to the following simplified configuration. Consider first a stage having three rotor blades and three stator blades. This configuration is shown in figure 5 in both axial and cascade projections. At time t_0 all rotor and stator blades are alined, whereas at time $t_0 + \Delta t$ the rotor has moved through a fraction of a revolution, and none of the blades are now alined. It is clear in this case that the geometric conditions which determine the flow through the stage are identical in each blade-to-blade passage at any time.¹ In this case the solution along an exterior grid row δ can be equated to that along the interior grid line β and similarly that along exterior line α can be equated to that along interior line γ at any instant. Consider now the case with three blades in the stator and four blades in the rotor as shown in figure 6. At time t_0 rotor blade 2 is alined with stator blade b, whereas at time $t_0 + \Delta t$ rotor blade 3 is alined with blade c. In this case the geometric conditions pertaining to the passage between blades a and b are obviously different from those for the passage between blades b and c at any time. However, it may be noted that those pertaining to passage bc at $t_0 + \Delta t$ are precisely the same as those which pertain to passage ab

¹It is assumed, of course, that the boundary conditions imposed at the inlet and discharge stations are spatially uniform so that the blade geometry provides the only scale for circumferential variations.

at the previous time t_0 . Therefore, the flow conditions along exterior grid line δ at time $t_0 + \Delta t$ can be equated to those along interior grid line β at the earlier time t_0 . However, in this case those along exterior grid line α at time $t_0 + \Delta t$ cannot be equated to those occurring in passage ab at time t_0 , but must be equated to those occurring along line γ at an earlier time. Thus a phase shift is introduced in application of the lateral boundary conditions. The necessary boundary information is acquired during the passage of time, and therefore the desired periodicity is attained asymptotically in time.

NUMERICAL EXAMPLE: BLADE-TO-BLADE PROGRAM

Results from the blade-to-blade program have been compared with data for a high-speed (1500-fps) fan tip section for which experimental data are reported in reference 8. The casing wall was instrumented with an array of fast response pressure gages, from which a contour plot of the rotating pressure field around the tip section was reconstructed. This fan was preceded by a set of guide vanes and followed by a row of stators. However, the unsteady interaction was neglected in this case and only the rotor was considered. The grid network was very coarse and consisted of 9 grid rows in the circumferential direction and 11 in the axial direction in each of 3 domains, that is, a total of 297 grid points.

The experimental pressure contour plot is reproduced on the left-hand side of figure 7. The data indicate the presence of an oblique shock off the leading edge of the upper blade which reflects off the lower blade and reimpinges on the upper blade near the trailing edge. A lambda (λ) type shock is apparently formed on the aft portion of the upper blade because of the boundary-layer separation. The isobars constructed from the numerical solutions are shown on the right-hand side of this figure. The numerical results exhibit qualitatively similar behavior, although boundary-layer effects have not been included and the grid is admittedly very coarse. Although a qualitative correlation is apparent with respect to the main features of the flow field, a quantitative comparison is somewhat difficult. Therefore, the experimental isobars have been used to construct pressure distributions along the suction and compression surfaces of the blade and along a mid-channel line. The accuracy of the data obtained in this manner may be somewhat suspect, but the agreement between the data and the numerical solution shown in figure 8 is considered to be very encouraging.

Numerical solutions for interacting blade rows have thus far been limited to idealized test case configurations for which no comparisons with other solutions or experimental data are available. However, results for the full stage consisting of fan and stator tip sections from reference 8 are included in reference 1.

HUB-TO-CASING ANALYSIS

Attention is now shifted to the second program, which considers a hub-to-casing stream surface. The coordinate system and grid network is illustrated in figure 9. The finite-difference grid lies on a meridional plane extending from hub to casing and from an inlet station to a discharge station. Circumferential variations are removed in this case by integration of the governing equations with respect to θ from one blade to the next and defining average properties over this angular interval. The angular velocity component and angular momentum equation are retained because of the presence of a pressure force exerted by the blades. The effects of blockage of the flow area due to the blade thickness and boundary-layer displacement thickness are included. Multiple blade rows can be considered but the effects of periodic interactions between the blade rows are necessarily neglected because of integration of the equations with respect to the angular variable.

In this analysis the basic system of equations given by equations (1) to (6) are stated in cylindrical coordinates, multiplied by $d\theta$ and integrated from $\theta_1(r,z)$ to $\theta_2(r,z)$, which are the surface coordinates of two adjacent blades, as indicated in figure 9. Outside a blade row, the integration interval is taken as $2\pi/N_i$. The blade-to-blade passage width is defined by

$$n = \begin{cases} N_i \int_{\theta_1}^{\theta_2} r \, d\theta & \text{(Within a blade row)} \\ 2\pi r & \text{(Outside a blade row)} \end{cases} \quad (30)$$

Circumferentially averaged values of the dependent variables are defined by

$$\hat{\rho} = n^{-1} N_i \int_{\theta_1}^{\theta_2} \rho r \, d\theta \quad (31)$$

$$\hat{\rho} \hat{v}_z = n^{-1} N_i \int_{\theta_1}^{\theta_2} \rho r v_z \, d\theta \quad (32)$$

It is assumed that the blades are thin and sharp and hence the local blade surface angles can be replaced by the mean camber line angles:

$$\frac{\partial \theta_1}{\partial z} \approx \frac{\partial \theta_2}{\partial z} = \frac{\partial \theta}{\partial z} \Big|_{\text{Camber line}} \quad (33)$$

$$\frac{\partial \theta_1}{\partial r} \approx \frac{\partial \theta_2}{\partial r} = \frac{\partial \theta}{\partial r} \Big|_{\text{Camber line}} \quad (34)$$

Furthermore, differences between root-mean-square (rms) values and mean squared values are neglected:

$$\left| \hat{v}_z^2 - \hat{v}_z^2 \right| \ll a^2 \quad (35)$$

$$\left| \hat{v}_r \hat{v}_z - \hat{v}_r \hat{v}_z \right| \ll a^2 \quad (36)$$

The following system of equations is thereby obtained²:

$$\frac{\partial(\rho n)}{\partial t} + \frac{\partial(\rho n v_z)}{\partial z} + \frac{\partial(\rho n v_r)}{\partial r} = 0 \quad (37)$$

$$\frac{\partial(\rho n v_z)}{\partial t} + \frac{\partial(\rho n v_z^2)}{\partial z} + \frac{\partial(\rho n v_r)}{\partial r} = -n \frac{\partial p}{\partial z} + \Delta p \left(r \frac{\partial \theta}{\partial z} \right) \quad (38)$$

$$\frac{\partial(\rho n v_r)}{\partial t} + \frac{\partial(\rho n v_r v_z)}{\partial z} + \frac{\partial(\rho n v_r^2)}{\partial r} = -n \frac{\partial p}{\partial r} + \frac{\rho n v_\theta^2}{r} + \Delta p \left(r \frac{\partial \theta}{\partial r} \right) \quad (39)$$

$$\frac{\partial(\rho n r v_\theta)}{\partial t} + \frac{\partial(\rho n r v_\theta v_z)}{\partial z} + \frac{\partial(\rho n r v_\theta v_r)}{\partial r} = -r \Delta p \quad (40)$$

$$\frac{\partial(\rho n E)}{\partial t} + \frac{\partial(\rho n v_z H)}{\partial z} + \frac{\partial(\rho n v_r H)}{\partial r} = -r \Omega \Delta p \quad (41)$$

where

$$\Delta p(r, z) = p(r, z, \theta_2) - p(r, z, \theta_1) \quad (42)$$

Thus the variable n represents the circumferential distance around the annulus, reduced by the cumulative blockage due to all blades, at fixed r and z . The term Δp represents the cumulative pressure differential across the blades, that is, the pressure differential across each blade times the number of blades. The terms involving Δp in the momentum equations represent the three components of the pressure force exerted by the blades. The term on the right-hand side of the energy equation is the work performed by the rotating blade row.

²The superscript notation to denote average quantities is dropped in the following discussion.

Within a blade row the velocity vector is assumed to remain tangent to the mean camber surface at all times:

$$v_{\theta} = \Omega r + v_z \left(r \frac{\partial \theta}{\partial z} \right) + v_r \left(r \frac{\partial \theta}{\partial r} \right) \quad (43)$$

The tangency condition is used within the blade rows to determine the angular velocity component, and the blade pressure differential Δp is obtained from the angular momentum equation. Outside the blade rows $\Delta p = 0$ and the angular momentum equation is used to determine the angular component of velocity.

Representation of the inlet and discharge boundary conditions and numerical solution of these boundary points follows the general approach described in connection with the blade-to-blade program. However, since a steady, rather than periodic, solution is sought in this case, somewhat less care need be taken in modeling a physically correct boundary condition. In particular, the "infinite duct" condition discussed previously has been replaced in this case by prescription of the total pressure at the inlet station. Similarly, prescription of the components vorticity of the incoming flow can be replaced by direct statement of the flow angles or of the radial and circumferential velocity components. At the discharge boundary the static pressure is specified. Solution at the boundary points along the hub and casing surfaces is accomplished by restating equations (37) to (41) in a body-oriented coordinate system similar to that used to derive equations (25) to (29). In this case, the boundary condition $\nabla = 0$ replaces the normal momentum equation. The same finite-difference procedure as used at the interior points is used to accomplish the solution of the remaining members of the system of equations. Noncentered differences are used for the derivatives normal to the walls, which only involve gradients of the normal velocity component. The accuracy of this procedure has been found to compare very well with that of the interior point solution, with considerable less complexity than the characteristic procedure used in the blade-to-blade program.

NUMERICAL EXAMPLES: HUB-TO-CASING PROGRAM

The present hub-to-casing program is analogous in many respects to the relaxation method program developed by Katsanis and McNally at NASA Lewis Research Center. Their program MERIDL (ref. 9) solves the stream function equation on a meridional plane through a blade row for steady subsonic conditions by use of a finite-difference method. The comparison between the present program and their program has been carried out for a case in which their solution should be very accurate. The rotor configuration selected corresponds to the test case used by Katsanis and McNally in reference 9.

The relative swirl angle is shown in figure 10. This angle is defined as that between the velocity vector and the projection of the velocity vector on a meridional plane, measured in a rotating frame of reference. The three curves pertain to the hub surface,

the tip or casing surface, and a mid-channel surface. Within the blade row the relative swirl angle along the hub and casing is completely determined by geometric constraints. However, everywhere else it is obtained from the solution for the three velocity components. The agreement between the two programs is considered to be quite satisfactory.

The magnitude of the velocity vector in the rotating frame is shown in figure 11. The mid-channel values were deleted from this figure for clarity. The only significant difference between the two solutions occurs near the leading edge. Both programs allow grid columns to cross the leading and trailing edges in an arbitrary fashion. However, Katsanis and McNally's program accounts for the effects of bluntness of the leading edge in some detail whereas the present program assumes that these edges are sharp.

Next, a transonic fan stage designed by NASA Lewis Research Center for the Quiet Fan Program has been considered. Designated the QF-1 stage it combines an 1100-fps tip speed rotor with a stator having highly "leaned" blades (up to 45° at the tip). A range of stator positions relative to the rotor location are possible with this stage; position VI was selected in this case. The rotor and stator are relatively close in this position, less than 1 chord length apart.

The pressure distributions along the hub and casing surface are shown in figure 12, and the absolute Mach numbers are displayed in figure 13. The supersonic region which develops in the stator along the hub, due to the combination of the hub curvature and blade thickness, is terminated by a normal shock. This shock is spread over about 4 or 5 grid points, or about 25 percent to 30 percent of the 16 grid points which cover the stator axially in this case. Only 10 grid points cover the rotor tip section; consequently, a shock in the rotor would be difficult to detect with the present grid point density. A rapid compression is evident on the aft portion of the rotor tip section, which corresponds to a reduction in relative Mach numbers from 1.12 near the leading edge to 0.64 at the trailing edge. Therefore, the rotor-tip compression substantially exceeds the normal-shock compression by itself.

COMPUTER EXECUTION TIME AND STORAGE REQUIREMENTS

The blade-to-blade program will fit in small-core memory of a CDC 7600 computer, that is, about 160K octal words, with a maximum of 1000 grid points (not including the exterior points required for the boundary point calculations), exclusive of the storage required for the periodic boundary data needed for unequal numbers of blades. In its present form, disk storage is used for the periodic boundary data, although use of the large-core memory would undoubtedly be more efficient. The blade-to-blade program requires approximately 2×10^{-4} second per grid point per time step for execution on a

CDC 7600 computer by using the FTN (opt = 2) compiler to generate the binary code. The results presented in figures 7 and 8 required less than 1 minute of execution time.

The hub-to-casing program also fits in small-core memory with a maximum of 1600 grid points. It requires approximately 4×10^{-4} second per grid point per time step for execution. The additional time relative to the blade-to-blade program is believed to be associated with calculation of the blade pressure differential Δp , solution of an additional momentum equation, and continuous reevaluation of the maximum permissible time step. (A variable time step is not allowed in the blade-to-blade program because of the procedure for storing and retrieving boundary data.) The subsonic rotor case discussed in connection with figures 10 and 11 required less than 1 minute of execution time with a 27 by 17 grid network. The transonic stage results shown in figures 12 and 13 required approximately 7 minutes of execution time.

CONCLUDING REMARKS

A blade-to-blade formulation and a hub-to-casing formulation have been developed for analysis of transonic unsteady flow through an axial turbomachine stage and implemented in two computer programs. Both employed an explicit finite-difference technique for solution at the interior grid points, and a characteristic type procedure at the inlet and discharge boundaries. The blade-to-blade program can treat periodic interactions between rotating and stationary blade rows, and particular attention has been given to correct representation of the blade slipstreams and their motion due to unsteady blade loading. A comparison with experimental measurements of the rotating pressure field of a high-speed fan tip section is considered to be very encouraging. The computer execution time for this case was very modest, less than 1 minute on a CDC 7600, and use of a higher grid point density to improve the numerical accuracy is therefore practical.

The hub-to-casing program compares favorably with a relaxation time solution for a flow condition when the latter should be very accurate. Results have also been obtained for a quiet fan stage which includes transonic flow in both the rotor and stator and a normal shock in the stator. The program resolves the shock reasonably well, although a higher grid point density would probably be beneficial in this case.

These programs offer a substantial improvement in the predictive capabilities available to aerodynamicists involved in design and evaluation of high-speed turbomachinery stages. However, it is clear that a complete description of the three-dimensional, unsteady, turbulent flow prevailing in such stages will require continued development of the computational models.

APPENDIX

ACOUSTIC FAR-FIELD ANALYSIS

Under the conditions typically prevalent in highly loaded transonic fan or compressor stages, the linearized, small-perturbation approximations to the equations of motion cannot be expected to be descriptive of the flow in the vicinity of the blades. Thus, recourse is made to the numerical solution of the complete nonlinear system of equations as discussed in connection with the blade-to-blade program. However, sufficiently far from the blade rows, the amplitude of the flow disturbances will decay to acoustic levels and the linearized, small-perturbation approximations will be descriptive of the far field. Therefore, an intermediate region in which both analyses are valid should exist at some distance from the blades. The inlet and discharge stations of the blade-to-blade computational domain can serve as the interfaces between the near-field (numerical) and far-field (acoustic) analyses. The present far-field analysis is formulated with respect to an infinite duct model, namely, outgoing waves should propagate without reflection. It differs, however, from conventional inlet duct analyses in that the signal may begin with an arbitrary transient, associated with the deviation of the assumed initial data in the near field from the periodic solution which is sought as the asymptotic limit in time. Therefore, the acoustic analysis must recognize that a transient signal will occur during startup and that a simple harmonic time dependence, which is the usual basis of inlet duct acoustics, cannot be assumed. The analysis should allow the transient to radiate outward without reflection, and should be capable of identifying the attainment of a periodic solution by the growth of discrete harmonic components in the solution.

The inlet and discharge stations indicated in figure 1 as the axial boundaries of domains 1 and 7 (or possibly of domains 2 and 6 if 1 and 7 are deleted) form the axial boundaries of the acoustic far field. However, the lateral boundary should extend over that fraction of the circumference which corresponds to the fundamental period of the stage configuration (that is, an integer number of blade-to-blade passages). This will require storage and retrieval of numerical data along this interface in the same manner as is performed along the interface between domains 4 and 5 of the near field.

As discussed in connection with the characteristic procedure used at the inlet and discharge boundaries, the compatibility relation on the outward running waves (eqs. (19) and (23)) provide a connection between the combination of pressure and axial velocity on the boundary points at time $t + \Delta t$ and the known interior point solution at time t . This information provides the mechanism for matching the acoustic far-field solution with the numerical near-field solution on a point-by-point, step-by-step basis. Since the blades are capable of producing a vorticity field which will convect downstream, additional information is necessary to define the downstream far field. (Recall that the inlet flow is

assumed to be irrotational.) If the standard small-disturbance approximations are employed, the numerical data to be provided at the inlet consist of

$$P(y,t) = \frac{p - p_{-\infty}}{\rho_{-\infty} a_{-\infty}} - (u - u_{-\infty}) \quad (A1)$$

and at the discharge station

$$Q(y,t) = \frac{p - p_{\infty}}{\rho_{\infty} a_{\infty}} + (u - u_{\infty}) \quad (A2)$$

$$R(y,t) = v \quad (A3)$$

where the subscripts denote the reference states at $x \rightarrow \pm\infty$, which are not necessarily the same. Equations (A1), (A2), and (A3) form, in effect, the boundary conditions for the far-field analysis, from which the instantaneous values of the pressure perturbation and velocity perturbation at the inlet and discharge stations are obtained.

With these preliminaries in hand, attention is now focused on the acoustic far-field analysis. In the following discussion the subscript $()_0$ will be used to denote the reference conditions for either boundary, that is, $x \rightarrow \pm\infty$, and all variables without subscript will refer to perturbations with respect to the reference state, namely, $p = p - p_0$ and $u = u - u_0$.

Since the present effort is addressed toward a cascade formulation, the governing equations are written in a two-dimensional Cartesian coordinate system. It is noted that the two-dimensional problem could be described by a solution of the wave equation alone, were it not for the fact that the time dependent force distribution on the blades is capable of producing a convected vorticity field (as well as a corresponding entropy field, which, however, is not relevant to the present problem). It will be seen that the convected vorticity field (characterized by a solenoidal velocity component) does not contribute to the acoustic pressure field by itself, as distinguished from the irrotational component of the velocity field which is directly coupled with the acoustic pressure. Therefore, the velocity perturbation field downstream of the discharge boundary station and upstream of the inlet boundary station is characterized by the sum of an irrotational velocity vector \bar{u}_1 and a solenoidal velocity vector \bar{u}_2 , which satisfy the linearized conservation equations³:

$$\frac{dp}{dt} + \rho_0 a_0^2 \nabla \cdot \bar{u} = 0 \quad (A4)$$

$$\rho_0 \frac{d\bar{u}}{dt} + \nabla p = 0 \quad (A5)$$

³Note that $u_2 = 0$ upstream of the inlet; however, the analysis is developed with respect to the more general case pertaining to the flow downstream of the discharge station.

$$\frac{dp}{dt} - a_0^2 \frac{d\rho}{dt} = \frac{p}{C_v} \frac{dS}{dt} = 0 \quad (\text{A6})$$

where

$$\nabla \times \bar{u}_2 = \omega \neq 0 \quad \frac{d}{dt} = \frac{\partial}{\partial t} + U \frac{\partial}{\partial x}$$

$$\nabla \cdot \bar{u}_2 = 0 \quad \bar{u}_1 = \bar{i}u_1 + \bar{j}v_1$$

$$\nabla \times \bar{u}_1 = 0 \quad \bar{u}_2 = \bar{i}u_2 + \bar{j}v_2$$

$$\bar{u} = \bar{u}_1 + \bar{u}_2 \quad U = M_0 a_0$$

It can be implied from these equations that solutions for p and \bar{u}_1 are purely radiative (propagating acoustically in a coordinate system convecting at the mean flow velocity U) whereas solutions for \bar{u}_2 are purely convective. These results can be expressed in terms of a Fourier integral representation:

$$\begin{Bmatrix} p(x,y,t) \\ u_1(x,y,t) \\ v_1(x,y,t) \end{Bmatrix} = \sum_n e^{-i\alpha_n y} \int_{-\infty}^{\infty} \begin{Bmatrix} \rho_0 a_0 A_n(\omega) \\ B_n(\omega) \\ C_n(\omega) \end{Bmatrix} e^{i(\omega t - \beta_n x)} \frac{d\omega}{2\pi} \quad (\text{A7})$$

$$\begin{Bmatrix} u_2(x,y,t) \\ v_2(x,y,t) \end{Bmatrix} = \sum_n e^{-i\alpha_n y} \int_{-\infty}^{\infty} \begin{Bmatrix} D_n(\omega) \\ E_n(\omega) \end{Bmatrix} e^{i\omega(t-x/U)} \frac{d\omega}{2\pi} \quad (\text{A8})$$

The boundary data can be expressed as

$$\begin{Bmatrix} P(y,t) \\ Q(y,t) \\ R(y,t) \end{Bmatrix} = \sum_n e^{-i\alpha_n y} \int_{-\infty}^{\infty} \begin{Bmatrix} \bar{P}_n^o(\omega) \\ \bar{Q}_n^o(\omega) \\ \bar{R}_n^o(\omega) \end{Bmatrix} e^{i\omega t} \frac{d\omega}{2\pi} \quad (\text{A9})$$

where a bar over a symbol denotes the time to frequency transform, and the superscript o indicates transformation from spatial location y to spatial harmonic n which will be discussed later.

Substitution of these integral forms into the governing equations gives

$$C_n = \frac{\alpha_n}{\beta_n} B_n \quad (\text{A10})$$

$$E_n = \frac{\omega}{U\alpha_n} D_n \quad (A11)$$

$$B_n = \frac{\hat{a}_0 \beta_n}{\omega - U\beta_n} A_n \quad (A12)$$

$$A_n + B_n + D_n = \bar{Q}_n^0 \quad (A13)$$

$$C_n + E_n = \bar{R}_n^0 \quad (A14)$$

The value of A_n , and thus B_n , C_n , D_n , and E_n , can thereby be expressed in terms of the transform of the boundary data as

$$A_n = \frac{\omega - U\beta_n}{\omega^2 + (a_0 - U)\beta_n\omega + Ua_0\alpha_n^2} (\omega\bar{Q}_n^0 + U\alpha_n\bar{R}_n^0) \quad (A15)$$

The propagation coefficient β_n is determined by substituting the integral relation for pressure into the convected wave equation as

$$\beta_n = \frac{-\omega M_0 \pm [\omega^2 - \alpha_n^2 a_0^2 (1 - M_0^2)]^{1/2}}{a_0 (1 - M_0^2)} \quad (A16)$$

where the + sign refers to downstream propagation (the discharge boundary) and the - sign to upstream propagation (the inlet boundary).

The selected representation of the solutions and boundary conditions as Fourier series in the y -direction is appropriate for enforcement of the periodicity boundary condition pertaining to spatial variations in this direction. The coefficient α_n is defined accordingly as

$$\alpha_n = \frac{2\pi n}{Y} \quad (A17)$$

where Y is the fundamental period of the stage cascade configuration. In addition, the fact that the boundary data are specified at a discrete number of grid points, say N , on the boundaries implies that the Fourier series can only include N terms, that is, $n = 0, 1, 2, \dots, N - 1$. Since the distance y to each point can be written as mY/N , where $m = 0, 1, 2, \dots, N - 1$ also, the Fourier series can be expressed in the standard Discrete Fourier Transform (DFT) notation:

$$\begin{Bmatrix} P(y,t) \\ Q(y,t) \\ R(y,t) \end{Bmatrix} = \begin{Bmatrix} P_m(t) \\ Q_m(t) \\ R_m(t) \end{Bmatrix} = \sum_{n=0}^{N-1} \begin{Bmatrix} P_n^0(t) \\ Q_n^0(t) \\ R_n^0(t) \end{Bmatrix} e^{-2\pi i n m / N} \quad (A18)$$

The inverse DFT is then

$$\begin{Bmatrix} P_n^o(t) \\ Q_n^o(t) \\ R_n^o(t) \end{Bmatrix} = \frac{1}{N} \sum_{m=0}^{N-1} \begin{Bmatrix} P_m(t) \\ Q_m(t) \\ R_m(t) \end{Bmatrix} e^{2\pi inm/N} \quad (\text{A19})$$

The desired solution for the pressure perturbation on the boundaries is accomplished after some manipulation as

$$p_m(t) = \rho_o a_o \sum_{n=0}^{N-1} e^{-2\pi inm/N} \begin{Bmatrix} H_n^o(t) * Q_n^o(t) + J_n^o(t) * R_n^o(t) \\ K_n^o(t) * P_n^o(t) \end{Bmatrix} \quad (\text{A20})$$

where $p_m(t)$ refers to the value at one of the N boundary grid points on the inlet or discharge boundary. Use of DFT techniques for $P_m(t)$, $Q_m(t)$, and $R_m(t)$ and similar DFT expansions for H_m , J_m , and K_m then leads to the convolution:

$$p_m(t) = \frac{\rho_o a_o}{N} \sum_{n=0}^{N-1} \begin{Bmatrix} H_n(t) * Q_{m-n}(t) + J_n(t) * R_{m-n}(t) \\ K_n(t) * P_{m-n}(t) \end{Bmatrix} \quad (\text{A21})$$

on the discharge and inlet boundaries, respectively. Thus a double convolution over both time and distance (in the y -direction) is required. The functions $P_m(t)$, $Q_m(t)$, and $R_m(t)$, therefore, represent the point sources of time-varying strength which are aligned along the considered boundaries, spatial resolution being consistent with the number of grid points specified. The functions $H_m(t)$, $J_m(t)$, and $K_m(t)$ are the duct response functions defined by

$$\begin{Bmatrix} H_m(t) \\ J_m(t) \\ K_m(t) \end{Bmatrix} = \sum_{n=0}^{N-1} \begin{Bmatrix} H_n^o(t) \\ J_n^o(t) \\ K_n^o(t) \end{Bmatrix} e^{-2\pi inm/N} = \begin{Bmatrix} \frac{1}{2} \delta(t) \\ 0 \\ \frac{1}{2} \delta(t) \end{Bmatrix} + \sum_{n=1}^{N-1} \begin{Bmatrix} H_n^o(t) \\ J_n^o(t) \\ K_n^o(t) \end{Bmatrix} e^{-2\pi inm/N} \quad (\text{A22})$$

$$H_n^o(\tau) = \frac{1}{n^2(1 - M_o^2)} \int_{-\infty}^{\infty} (\Omega - T_n) \Omega e^{i\Omega\tau} \frac{d\Omega}{2\pi} \quad (\text{A23})$$

$$J_n^o(\tau) = \frac{1}{n(1 - M_o^2)} \int_{-\infty}^{\infty} (\Omega - T_n) e^{i\Omega\tau} \frac{d\Omega}{2\pi} \quad (\text{A24})$$

$$K_n^o(\tau) = \frac{1}{n(1 - M_o^2)(1 + M_o)} \int_{-\infty}^{\infty} (\Omega - T_n)(\Omega + M_o T_n) e^{i\Omega\tau} \frac{d\Omega}{2\pi} \quad (A25)$$

where δ is the Dirac delta function and

$$T_n = \left[\Omega^2 - (1 - M_o^2)n^2 \right]^{1/2}$$

$$\Omega = \frac{\omega}{\alpha} a_o$$

$$\tau = \frac{\alpha}{a_o t}$$

$$\alpha = \frac{2\pi}{Y}$$

A group of subroutines including an efficient Fast Fourier Transform routine has been developed for use in conjunction with the blade-to-blade computer program to carry out the indicated convolutions numerically. Results have been thus far limited to test cases with a simple harmonic input signal. For example, in one of the calculations the discharge station was assumed to be divided into 8 intervals covering a total circumferential distance of 0.1 foot. The selected reference (average) Mach number of the discharge flow was 0.8. The flow was assumed to be irrotational so that only one input function $Q(y,t)$ was required, and the second input function $R(y,t)$ could be considered as a response function (that is, it was calculated from $Q(y,t)$). The input function $Q(y,t) = \cos\left(\Omega\tau - \frac{2\pi n}{N}\right)$, with $Q(y,t) = 0$ for $\tau < 0$, was selected for this case, where $\tau = 2\pi Na_o t / Y$, $n = 1, 2, \dots, N$, $N = 8$, $Y = 0.1$ foot, $a_o = 10^3$ fps, and $\Omega = 1$. The input function Q and response function R at $n = 1$ are plotted in figure (A1). It should be noted that the response function is initially out of phase with the input function because of the assumption that $Q = 0$ for $\tau < 0$. However, the effect of the transient at $\tau = 0$ dies quickly, and after about 1/3 millisecond the response function closely approximates the input function and indicates the desired harmonic solution is being approached asymptotically. The nondimensional perturbation pressure is plotted in figure (A2). The complete history is shown for the point $n = 1$, whereas the history of the points $n = 2$ and 3 is only shown at early times, where a difference in amplitude as well as phase exists. At later times (that is, after about 1/3 millisecond) the pressure solutions at the various grid points only differ noticeably by the phase angle corresponding to the input function, as the differences in amplitude asymptotically decay.

REFERENCES

1. Alzner, Edgar; and Erdos, John: Computation of Unsteady Transonic Flows Through Rotating and Stationary Cascades. Volume 1 - Method of Analysis. ATL TR 205 (Contract No. NAS 3-16807), Advanced Technology Labs., Inc., May 1975.
2. Vavra, Michael H.: Aero-Thermodynamics and Flow in Turbomachines. John Wiley & Sons, Inc., 1960.
3. Katsanis, Theodore: FORTRAN Program for Calculating Transonic Velocities on a Blade-To-Blade Stream Surface of a Turbomachine. NASA TN D-5427, 1969.
4. MacCormack, Robert W.: Numerical Solution of the Interaction of a Shock Wave With a Laminar Boundary Layer. Proceedings of the Second International Conference on Numerical Methods in Fluid Dynamics, Vol. 8 of Lecture Notes in Physics, Maurice Holt, ed., Springer-Verlag, 1971, pp. 151-163.
5. Kemp, Nelson H.; and Sears, W. R.: Aerodynamic Interference Between Moving Blade Rows. J. Aeronaut. Sci., vol. 20, no. 9, Sept. 1953, pp. 585-612.
6. Moretti, Gino; and Abbett, Michael: A Time-Dependent Computational Method for Blunt Body Flows. AIAA J., vol. 4, no. 12, Dec. 1966, pp. 2136-2141.
7. Serra, Raymond A.: Determination of Internal Gas Flows by a Transient Numerical Technique. AIAA J., vol. 10, no. 5, May 1972, pp. 603-611.
8. Bilwakesh, K. R.; Koch, C. C.; and Prince, D. C.: Evaluation of Range and Distortion Tolerance for High Mach Number Transonic Fan Stages. Final Report on Task II: Performance of a 1500 Feet per Second Tip Speed Transonic Fan Stage With Variable Geometry Inlet Guide Vanes and Stator. NASA CR-72880, 1972.
9. Katsanis, Theodore; and McNally, William D.: FORTRAN Program for Calculating Velocities and Streamlines on the Hub-Shroud Mid-Channel Flow Surface of an Axial- or Mixed-Flow Turbomachine. I - User's Manual. NASA TN D-7343, 1973.

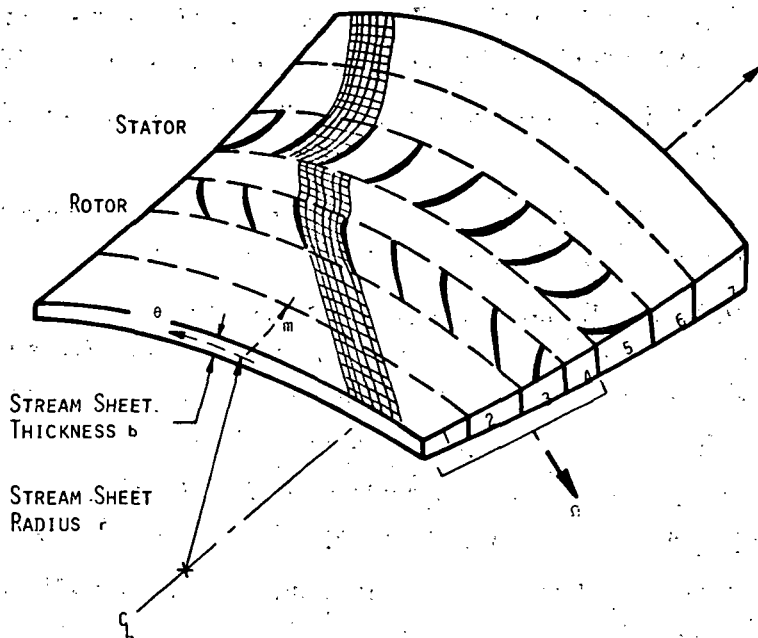


Figure 1.- Blade-to-blade coordinate system and grid network.

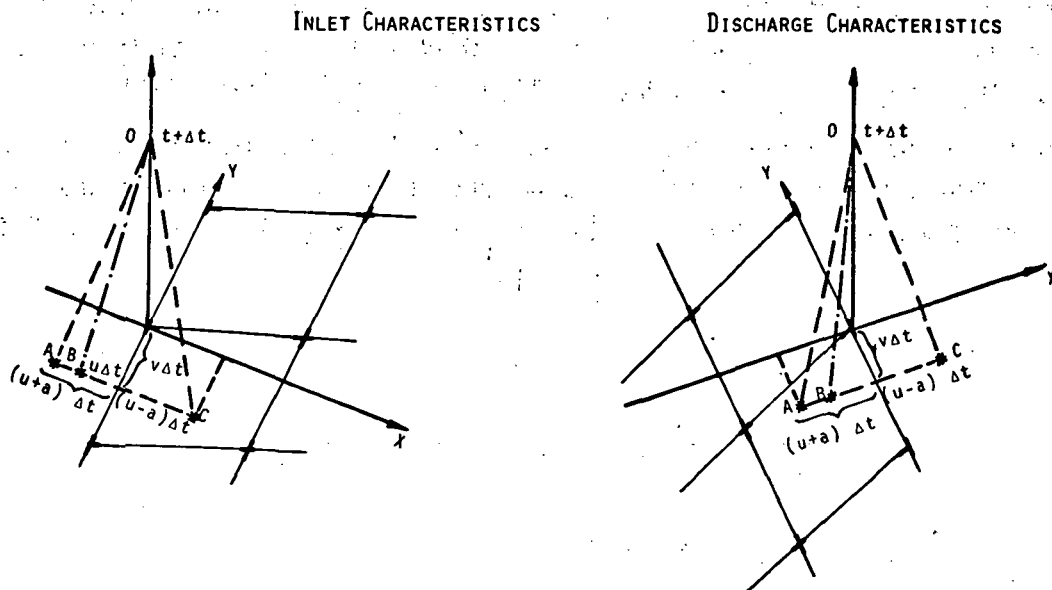


Figure 2.- Characteristic surfaces and grid points at inlet and discharge stations.

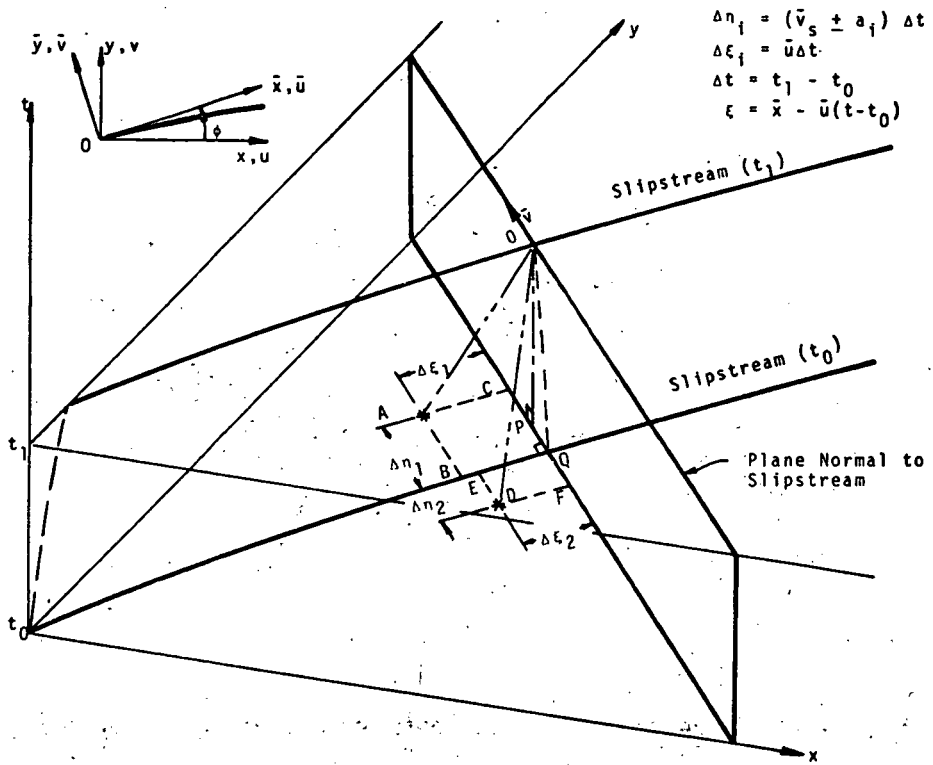


Figure 3.- Slipstream and blade surface characteristic geometry.

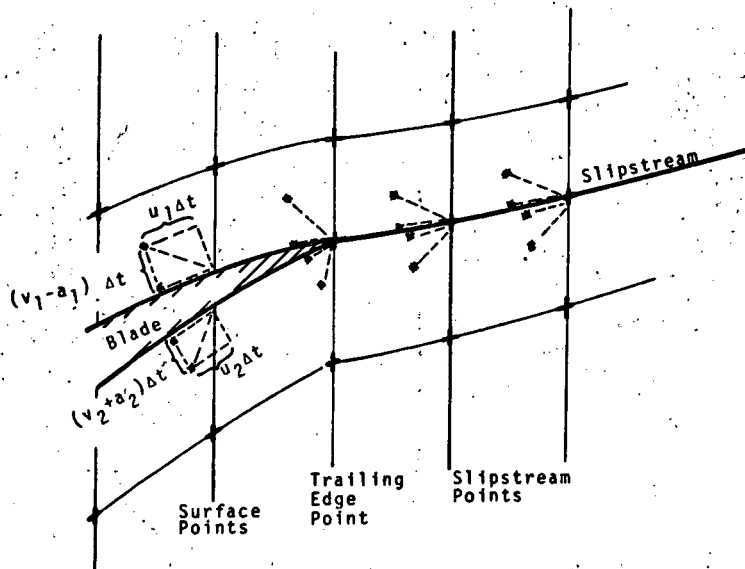


Figure 4.- Blade and slipstream characteristic system.

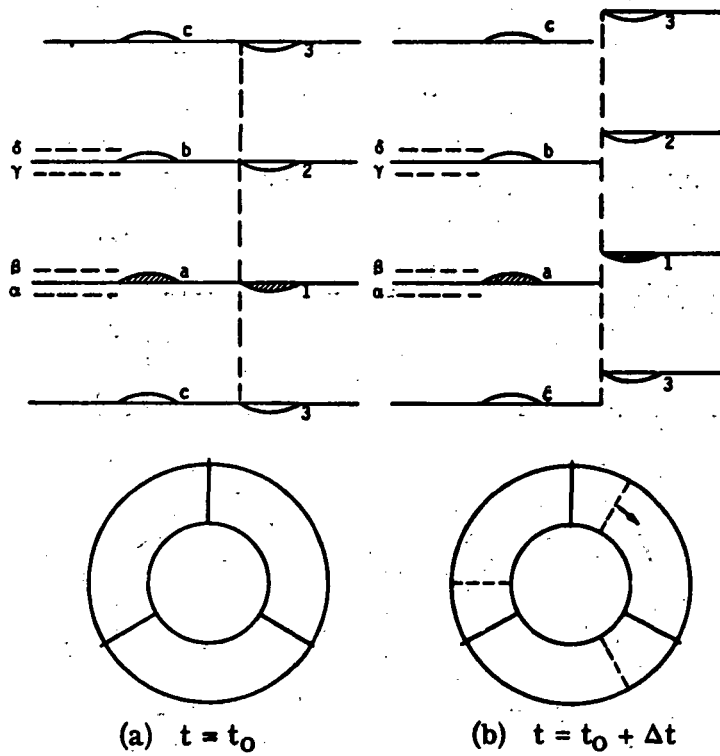


Figure 5.- Illustration of cyclic algorithm for stage with equal number of blades in stator and rotor. $N_1 = 3$, $N_2 = 3$.

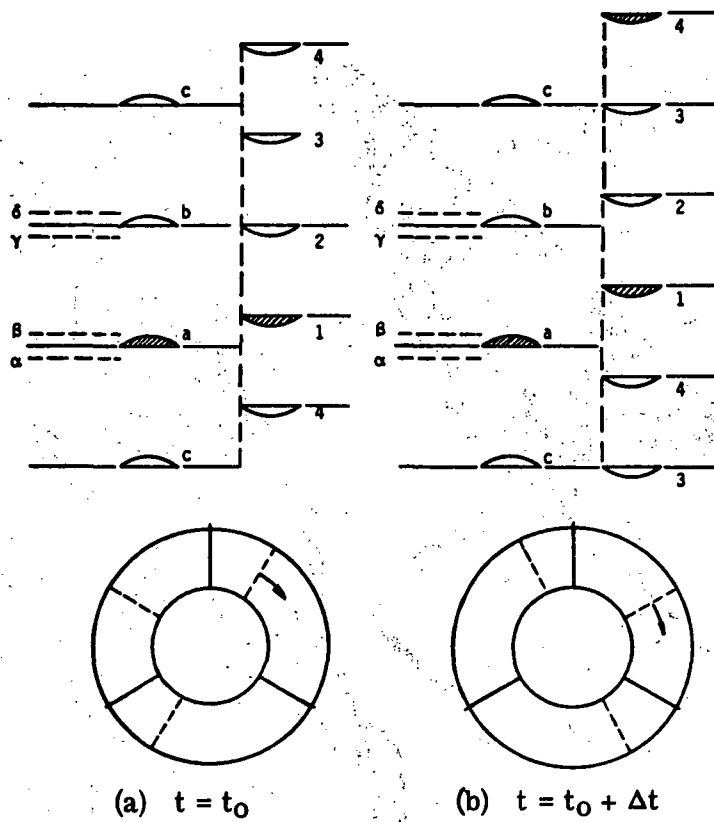


Figure 6. - Illustration of cyclic algorithm for stage with unequal number of blades in stator and rotor. $N_1 = 3$, $N_2 = 4$.

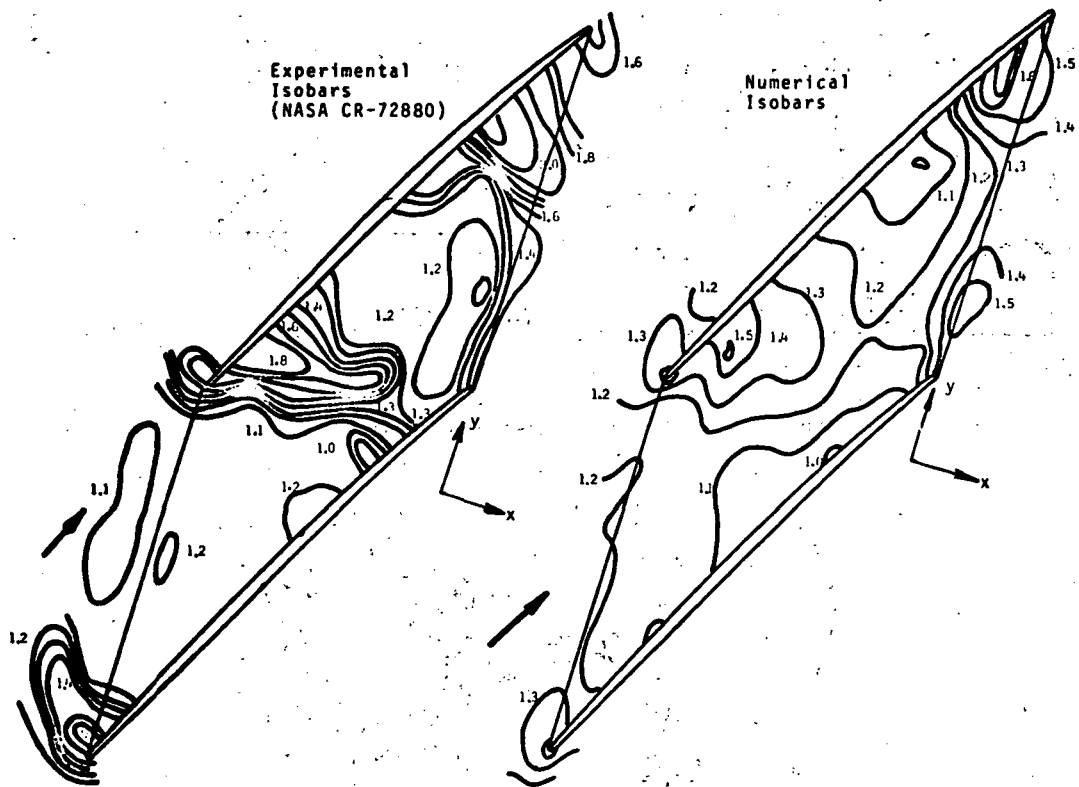


Figure 7.- Comparison of experimental and numerical pressure distributions for 1500 fps rotor.

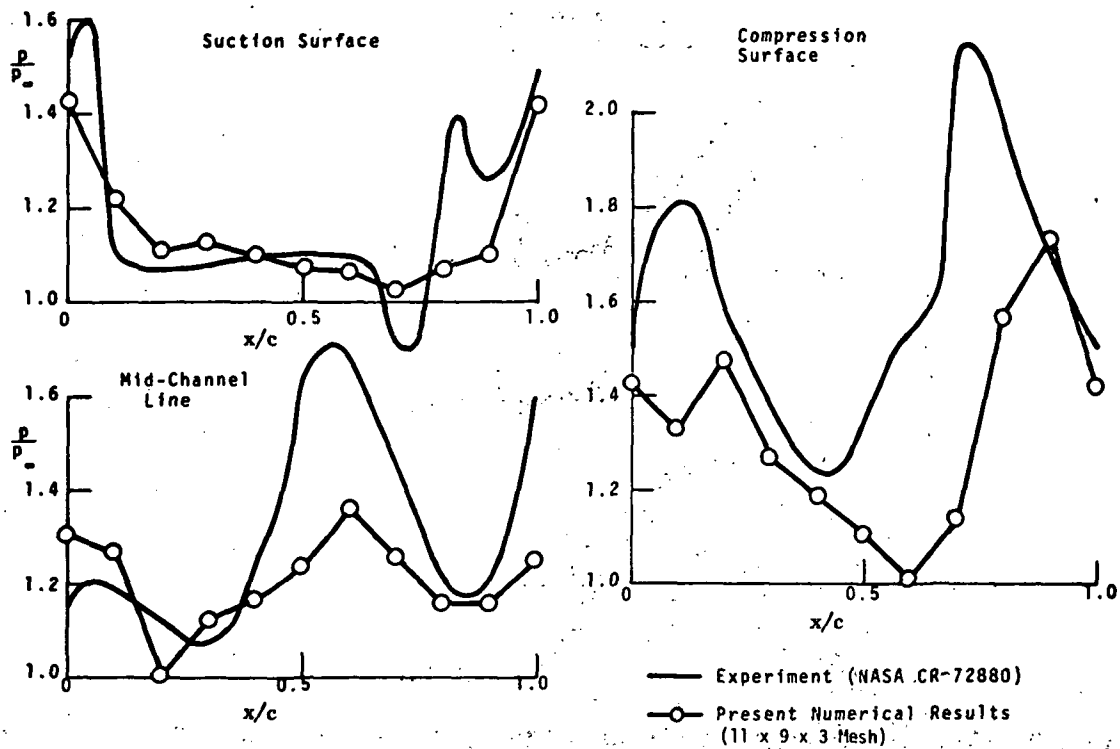


Figure 8. - Rotor pressure distributions.

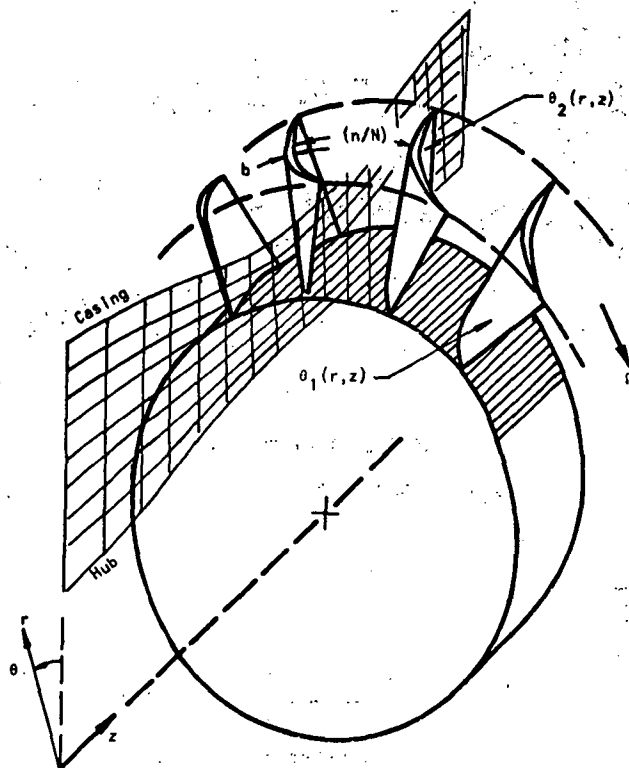


Figure 9. - Hub-to-casing coordinate system and grid network.

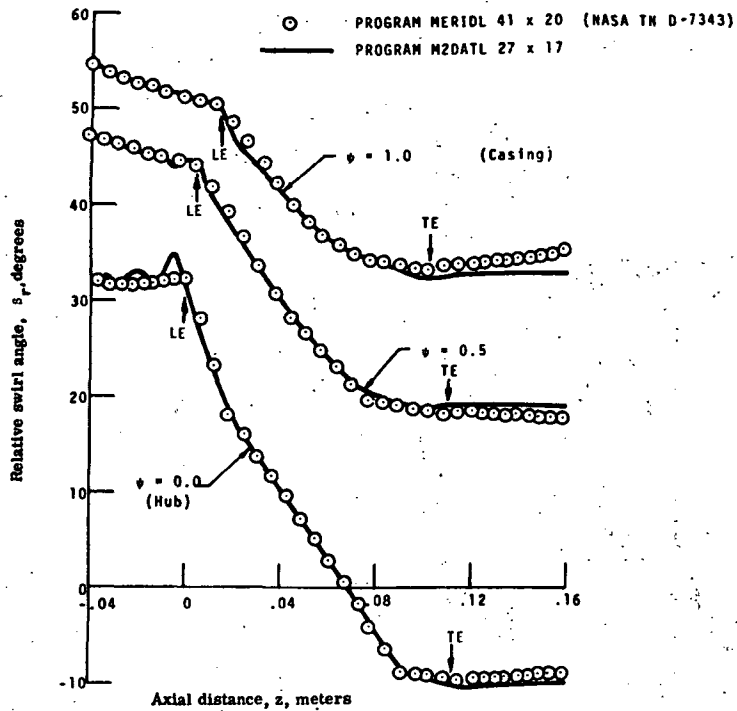


Figure 10.- Comparison of relative swirl angle variations through a subsonic rotor.

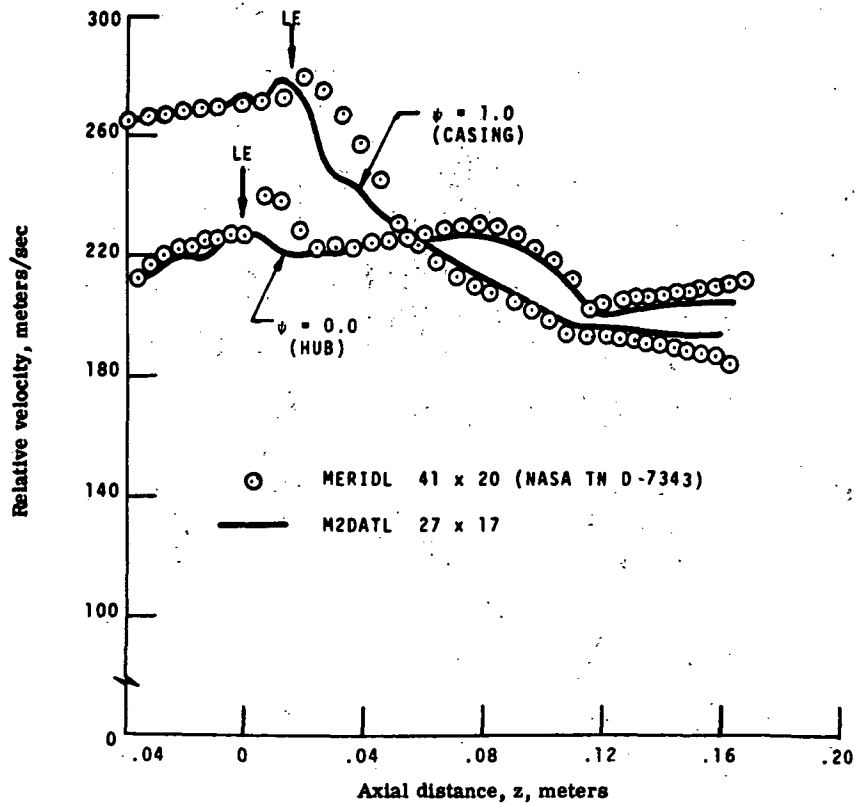


Figure 11.- Comparison of relative velocity distributions through a subsonic rotor.

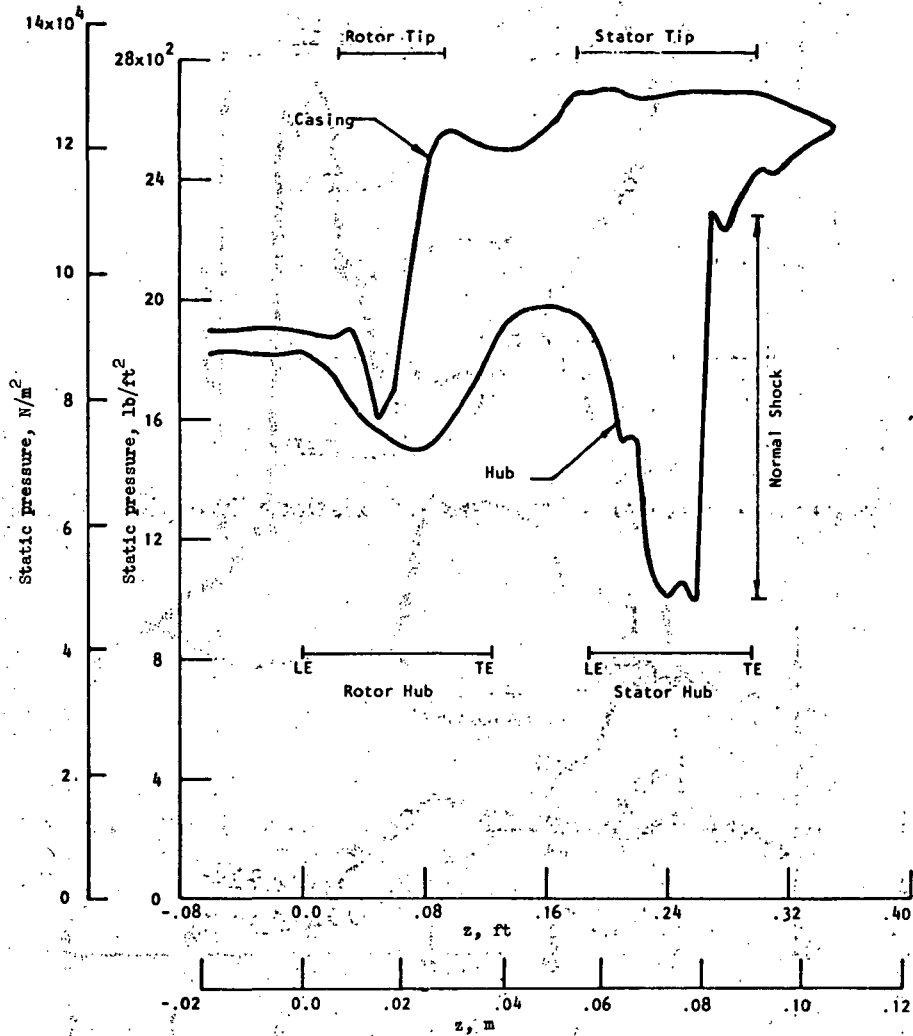


Figure 12.- Variation of static pressure along hub and casing through NASA QF-1 stage.
 Rotor 15; stator S9D Δ 45^o; position VI.

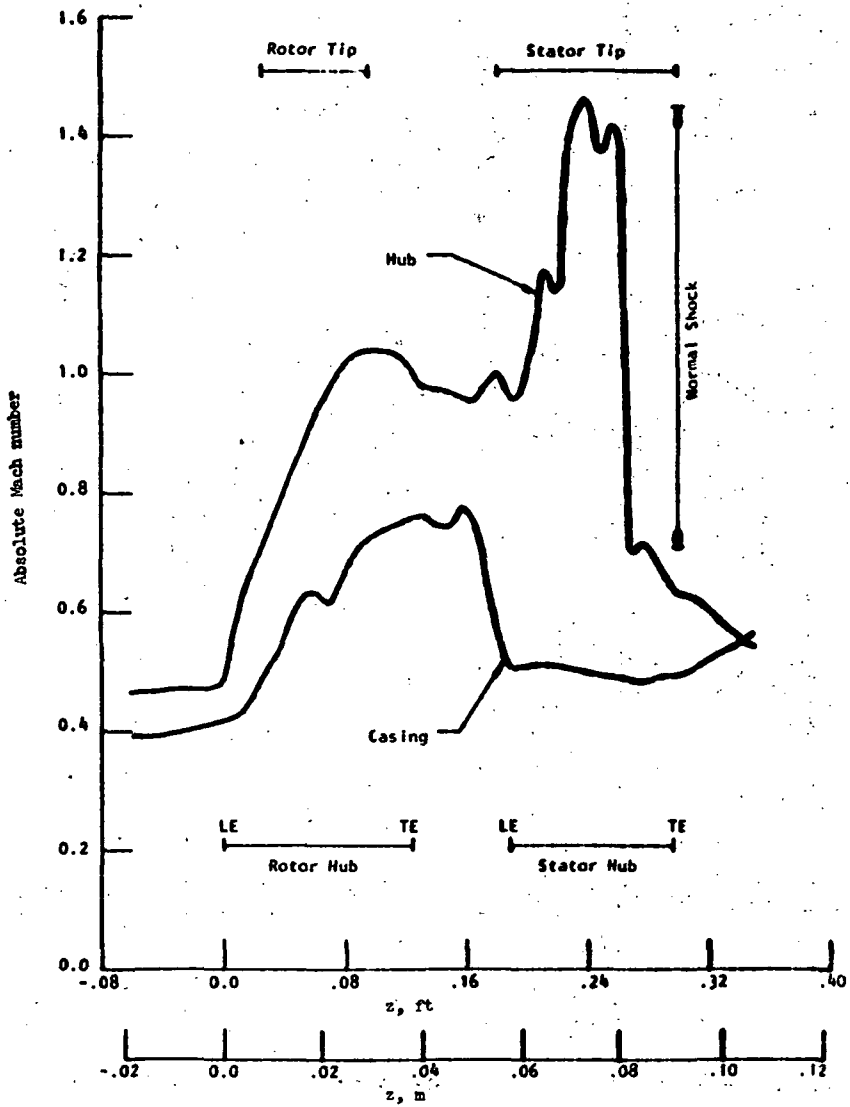


Figure 13.- Variation of Mach number along hub and casing through NASA QF-1 stage.

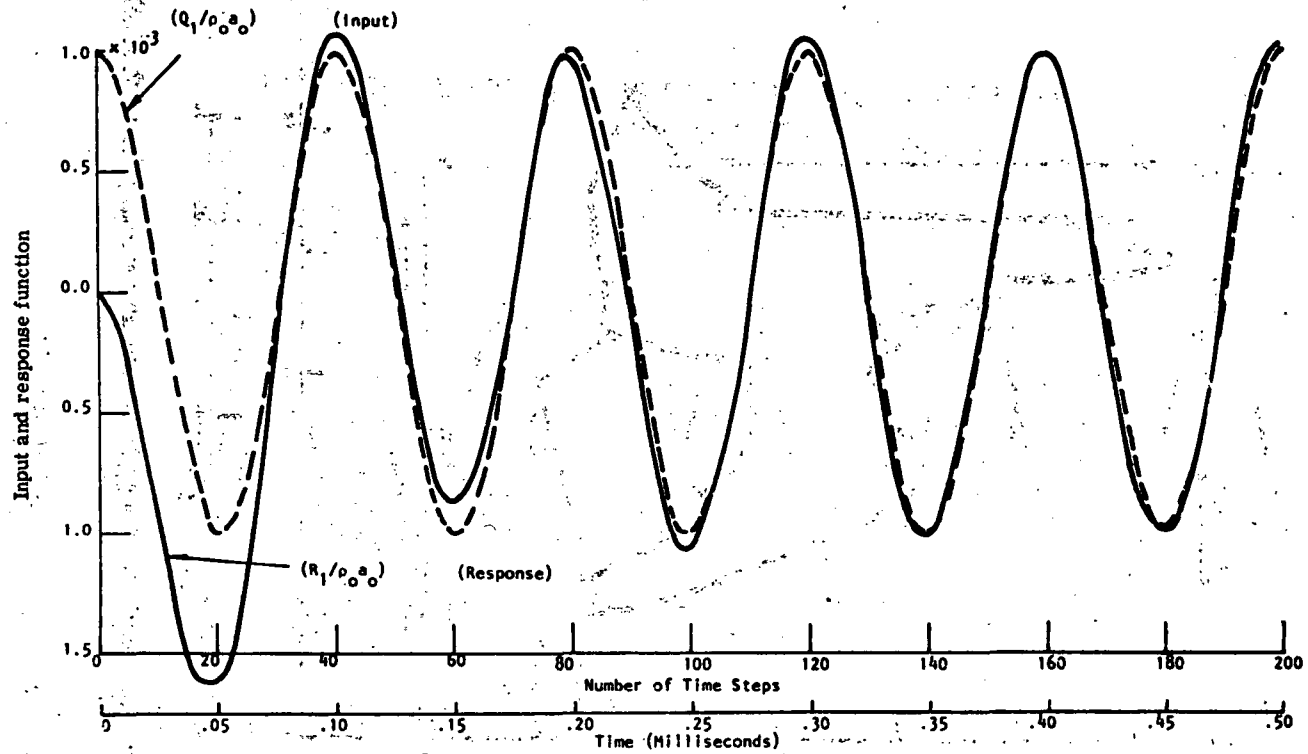


Figure 14. - Input and response functions for test cases.

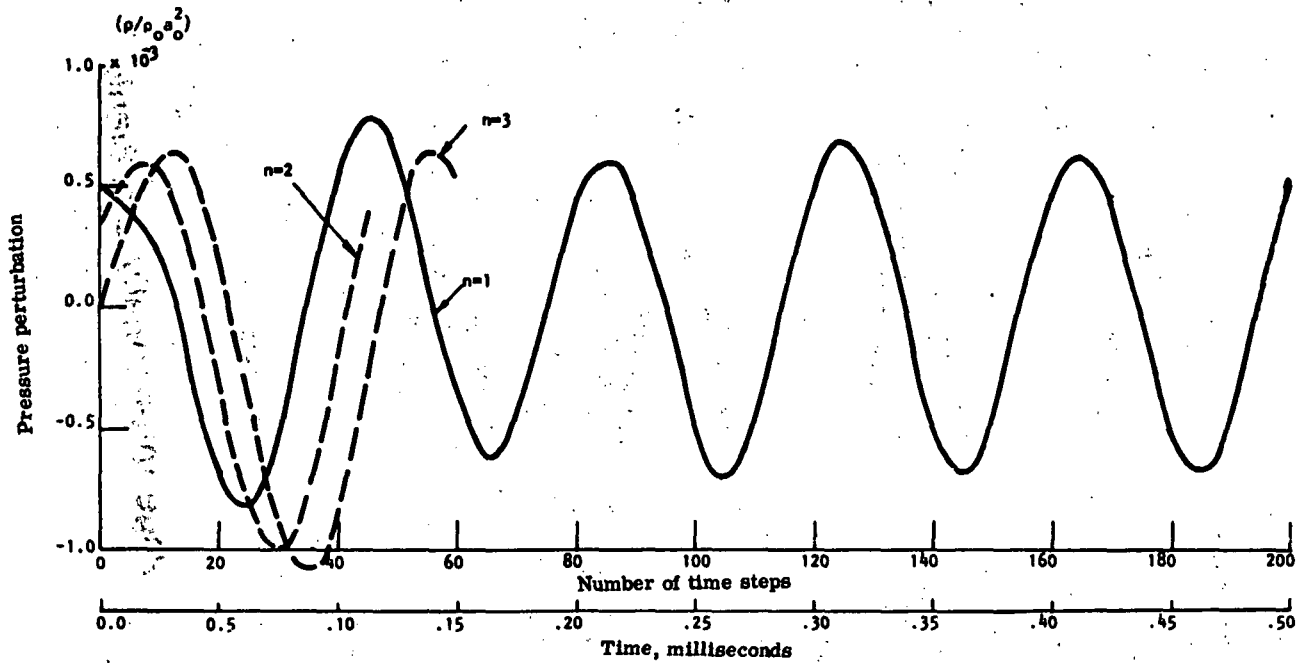


Figure 15. - Pressure perturbations at several grid points.